Can. J. Remote Sensing, Vol. 31, No. 1, pp. 61–72, 2005

Classification of fully polarimetric single- and dual-frequency SAR data of sea ice using the Wishart statistics

Bernd Scheuchl, Ian Cumming, and Irena Hajnsek

Abstract. Information on the extent and composition of sea ice is important for shipping and offshore operations. Single-polarization spaceborne synthetic aperture radar (SAR) data are an important information source for ice centres around the world. Next-generation SAR satellites will have the capability to collect fully polarimetric SAR data. In this paper we analyze the differences between polarimetric signatures of sea ice and those of land, test several applications of an unsupervised segmentation based on the Wishart distribution of polarimetric data, and give recommendations for modifications to the segmentation method. Airborne C- and L-band sea ice data are investigated. Surface scattering largely dominates sea ice backscatter. A volume component is present; it only dominates for some regions of selected ice types depending on the radar frequency. Dihedral scattering rarely dominates. The application of speckle filters further reduces the number of pixels with predominantly double bounce. The separation of scattering characteristics using the Freeman–Durden model before image classification provides little additional information. The initialization of the segmentation method with a scattering strength based classifier is very efficient and leads to good results.

Résumé. L'information sur l'étendue et la composition des glaces est importante pour la navigation et les opérations au large. Les données RSO à polarisation unique constituent une importante source d'information pour les centres des glaces autour du monde. Les satellites RSO de la prochaine génération auront la capacité d'acquérir des données polarimétriques RSO. Dans cet article, nous analysons les différences dans les signatures polarimétriques de la glace par rapport à celles de la terre ferme, nous testons plusieurs applications d'une segmentation non dirigée basée sur la distribution de Wishart de données polarimétriques et nous formulons des recommandations pour des modifications éventuelles. Nous examinons les données aéroportées en bande C et L de la glace de mer. La diffusion de surface domine largement la diffusion de la glace de mer. Une composante du volume est présente; elle domine uniquement dans certaines régions présentant des types de glace déterminés en fonction de la fréquence radar. La diffusion dièdre domine rarement. L'application de filtres de chatoiement réduit encore davantage le nombre de pixels caractérisés pas le phénomène de seconde réflexion. La séparation des caractéristiques de diffusion à l'aide de la technique de Freeman–Durden avant la classification de l'image fournit peu d'information additionnelle. L'initialisation de la méthode de segmentation par un classificateur basé sur la puissance de diffusion est très efficace et entraîne de bons résultats.
[Traduit par la Rédaction]

Introduction

Sea ice coverage of the polar oceans and their adjacent seas is of interest for scientific as well as economic reasons. Sea ice is part of the cryosphere and plays an important role in the global climate system. Ship traffic and offshore operations are affected in ice-infested waters, causing an economic impact because of delays, route changes, or temporary shutdowns of operations for safety reasons. Accurate knowledge about the extent and composition of sea ice is needed. Many countries whose waterways are affected by sea ice have established ice monitoring centres to maintain knowledge of ice conditions and sea ice climatology. In Canada, the Canadian Ice Service (CIS) provides daily ice charts for Canadian waters among other products.

The vast extent of the area affected, in combination with its often remote location, makes satellite remote sensing the method of choice for sea ice monitoring. Spaceborne synthetic aperture radar (SAR) instruments are most useful for the task because they are independent of daylight and cloud cover. The launch of RADARSAT-1 marks a milestone for operational sea ice monitoring around the world and currently provides the primary data for the CIS.

One of the difficulties in sea ice monitoring is the variability of both ocean and ice signatures with local and seasonal conditions, which makes image interpretation a challenge. Single-polarization SAR data, as provided by RADARSAT-1, show limitations in the separation of open water and sea ice when environmental conditions are such that the backscatter

Received 30 April 2004. Accepted 8 October 2004.

B. Scheuchl[1] **and I. Cumming.** Department of Electrical and Computer Engineering, University of British Columbia, 2356 Main Mall, Vancouver, BC V6T 1Z4, Canada.

I. Hajnsek. Department of SAR Technology, Microwaves and Radar Institute, German Aerospace Center e.V. DLR, PO Box 1116, Wessling 82230, Germany.

[1]Corresponding author. Present address: MacDonald Dettwiler and Associates Ltd., 13800 Commerce Parkway, Richmond, BC V6V 2J3, Canada (e-mail: bscheuch@mda.ca).

signatures of open ocean are similar to those of sea ice (Scheuchl et al., 2004). Operations at the CIS therefore rely heavily on expert human analysts to interpret the data available and produce ice charts that indicate the location of sea ice and more detailed information on ice types and ice concentrations.

The ENVISAT ASAR already offers acquisition modes with two polarizations. Future missions like ALOS PALSAR (L-band), RADARSAT-2 (C-band), and TerraSAR (X- and L-band) will provide fully polarimetric acquisition modes. These next-generation SAR satellites offer the opportunity to collect fully polarimetric SAR data over one or more ice seasons, thus providing the basis for research to gain a better understanding of polarimetric sea ice signatures. Because of power constraints and data-rate limitations, the swath widths for fully polarimetric modes are limited and will not provide sufficient coverage for operational sea ice monitoring.

Multipolarization data are acknowledged to provide increased information content (Nghiem and Bertoia, 2001). Airborne fully polarimetric data have been found to show potential for sea ice classification (Drinkwater et al., 1992; Rignot et al., 1992). In this paper, we investigate the capabilities of an unsupervised segmentation method based on the Wishart distribution of polarimetric data for sea ice classification. A number of seed options for the segmentation method are evaluated for L- and C-band data. The interpretation of results based on various polarimetric parameters is also discussed.

The next section of the paper discusses radar backscatter from sea ice and describes the polarimetric data available for this project. In subsequent sections, classification methods and application-specific modifications are discussed, classification results are analyzed, and conclusions are drawn.

Polarimetric SAR data of sea ice

Few fully polarimetric SAR scenes of sea ice have been collected to date. The data available do not cover extensive areas, and no data cover a specific area over a full ice season.

During two missions in April and October 1994, the shuttle imaging radar (SIR-C) provided spaceborne fully polarimetric SAR data from sea ice. Data acquired over the Weddell Sea were analyzed by Erikkson et al. (1998), and Scheuchl et al. (2001) investigated data acquired off the coast of Newfoundland. Both datasets lack ground validation.

Until the launch of spaceborne SAR sensors with fully polarimetric capability, airborne polarimetric SARs are the most important data source for research purposes. Of the numerous sensors available, the Danish EMISAR, Canadian CV-580, Japanese PI-SAR, and American NASA JPL AirSAR were used to acquire polarimetric SAR data from sea ice in the Northern Hemisphere. In this paper, we investigate data acquired in 1988 by the JPL AirSAR in the Beaufort Sea.

Backscatter from sea ice

For sea ice the total backscatter is a combination of surface (potentially including specular reflection), volume, and dihedral scattering. Dihedral scattering (double bounce) can occur on ridges, where the ridging causes natural corners. As discussed later in the paper, this component is rather small compared with the other two scattering mechanisms. Sea ice backscatter is generally lower than backscatter from land. In addition, the variation of the mixture of mechanisms is not as great, making classification more challenging.

Surface scattering dominates backscatter from first-year ice (FYI). It occurs on the boundary between two media (i.e., air–ice). If the ice surface is rough with respect to the wavelength, the signal is scattered back to the source; from a smooth surface the signal is scattered away from the source (little to no backscatter). Specular reflection can happen for very steep incidence angles, resulting in high backscatter. This phenomenon is not investigated here.

Volume scattering is mainly caused by dielectric discontinuities in the medium. For multiyear ice (MYI), the number of inhomogeneities in the ice sheet increases. The upper part of MYI generally consists of low-density layers with millimetre-sized air bubbles. These volume inhomogeneities interact stronger with C-band than with L-band (Hallikainen and Winebrenner, 1992). For C-band, the volume scattering of the MYI component is significant. The longer L-band wavelength interacts with fewer inhomogeneities (i.e., fewer inhomogeneities are in the order of the radar wavelength), resulting in low-volume backscatter for MYI. Volume scattering can occur in deformed and ridged ice for both frequencies.

AirSAR data acquired in the Beaufort Sea

In 1988 the NASA JPL conducted an extensive sea ice research program in the Beaufort Sea. A floating ice camp was set up to obtain in situ measurements, including ice profiles and meteorological data. In addition, the airborne AirSAR acquired several datasets in the area. Polarimetric SAR data were acquired in C-, L-, and P-band. The sensor noise level is given as –40 dB at 40° incidence for L- and P-band and –35 dB for C-band. The data were subsequently subject to detailed investigation, and numerous publications are available on the topic (Drinkwater et al., 1991; Rignot and Drinkwater, 1994; Kwok et al., 1995; Winebrenner et al., 1995), making this acquisition the single most important to date.

Scene 1372 is used for this study and was acquired on 11 March 1988, with scene centre coordinates of 73.048°N and 142.285°W and incidence angle variation from 22° to 52°. With respect to the upcoming spaceborne missions, this paper focuses on L- and C-band data only. Rignot and Drinkwater (1994) suggest that P-band data are similar to L-band data with a reduced contrast between FYI and MYI and are therefore not considered particularly useful for ice mapping.

Figures 1a and **1b** show colour representations for the four-look C- and L-band data, respectively. A number of ice types

that can be identified in the scene are labelled in **Figure 1b**. The size of the test site is approximately 6.6 km (range) and 12.1 km (azimuth). The area does not cover the ice camp location but was close enough to assume that similar ice conditions were present.

In and around the camp a mixture of FYI and MYI floes is reported. The average thickness of the FYI near the ice camp was reported to be between 1.5 and 2.4 m. MYI floes were hummocked to amplitudes up to 6 m and are surrounded by compressed FYI. A layer of dry snow with an average thickness of 15 cm is reported. The SAR data were acquired at a temperature below –10 °C and wind speed below 5 m/s (Rignot and Drinkwater, 1994).

The large floes appearing bright in the C-band image (**Figure 1a**) and purple in the L-band image (**Figure 1b**) are MYI. Compressed first-year ice (CFYI) surrounds the MYI floes and is best visible in the L-band image where it appears white (**Figure 1b**). The L-band image shows good contrast between ice with a rough surface (compressed and ridged) and ice with a smoother surface. In comparison, the C-band image does not show good contrast between CFYI and MYI. The web of bright lines in both images indicates rough and deformed FYI (RFYI) and first-year rubble and ridges (FYIRR). Dark purple areas are smooth FYI (SFYI), and the black features indicate leads that opened in the ice due to dynamic forces. The classification is based on results from a previous study (Rignot and Drinkwater, 1994). Kwok et al. (1995) and Winebrenner et al. (1995) suggest that the leads are already covered with thin ice (ThI).

Data classification

In the literature, the terms segmentation and classification are frequently used with overlapping meaning. In this paper, segmentation refers to the clustering of pixels into subsets according to given metrics, and classification requires the identification of the nature of the segmented clusters.

Based on this definition, the term unsupervised classification would therefore mean no human interaction for the entire process. In the literature, however, unsupervised classification often refers to methods that require result interpretation. The method investigated here (also referred to as the Wishart classifier) is an unsupervised segmentation; the assignment of segments to ice types (the classification) is a required manual task. No conclusions on general validity can be drawn from a single scene; this aspect is not investigated here for lack of a representative dataset.

Dominant scattering mechanism based on the Freeman–Durden model

The availability of polarimetric SAR data allows the analysis of the scattering mechanisms involved. This in itself is a form of classification; however, the result is interpreted based on scattering mechanisms rather than ice types. **Figures 2a** and **2b** show dihedral–volume–surface (RGB) colour composite images for C- and L-band, respectively, using the double-bounce, volume, and surface scattering components. The contributions of the various scattering mechanisms were derived using the Freeman–Durden decomposition (Freeman and Durden, 1998). Both images appear mostly blue, indicating the dominance of surface scattering.

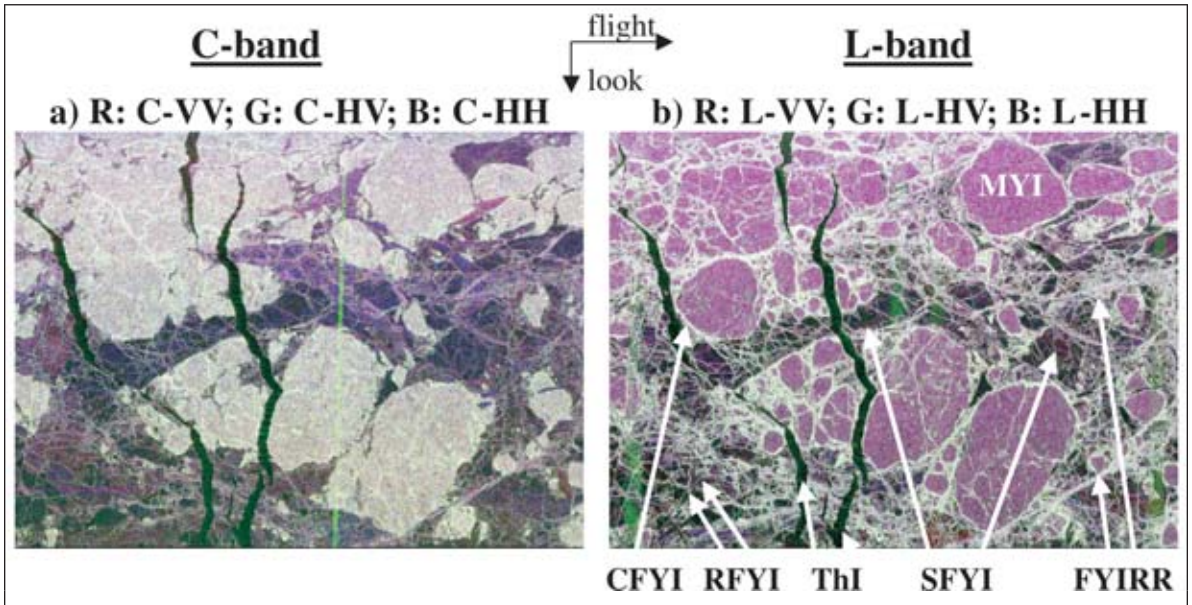

Figure 1. RGB colour composite images for scene 1372 acquired by NASA JPL AirSAR on 11 March 1988 in the Beaufort Sea. The image dimensions are approximately 6.4 km in range and 12 km in azimuth, and the incidence angle range is about 22°–54°. CFYI, compressed first-year ice; FYIRR, first-year rubble and ridges; RFYI, rough and deformed first-year ice; MYI, multiyear ice; SFYI, smooth first-year ice; ThI, thin ice.

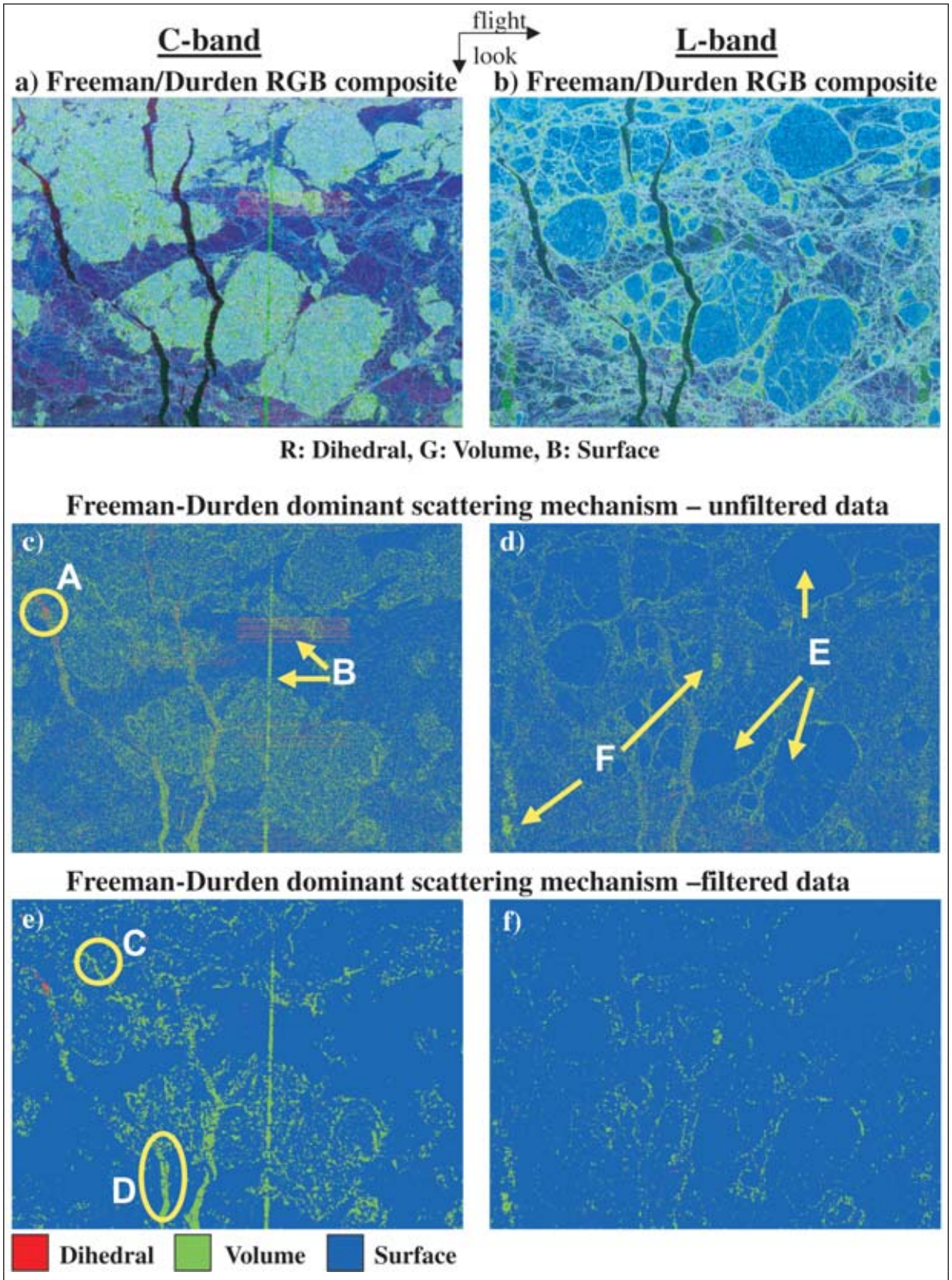

Figure 2. Freeman–Durden scattering mechanisms. (a, b) RGB colour composite images. (c–f) Classification results based on dominant scattering mechanism (surface scattering, volume scattering, or double bounce). A, lead with dihedral signature; B, linear features due to processing or instrument error; C, CFYI; D, leads; E, MYI; F, CFYI.

The Freeman–Durden decomposition can be interpreted as an unsupervised classifier. **Figures 2c–2f** show the dominant scattering mechanism for C- and L-band for the original four-look data and filtered data. The four-look data were filtered using the edge-preserving filter proposed by Lee et al. (1999a) and a filter window size of five, resulting in an equivalent number of looks (ENL) of 60.

Dihedral scattering (shown in red) dominates only a very small portion of the data, mostly in ridged areas. One exception is a lead region for C-band (see A in **Figure 2c**). The red horizontal and green vertical linear features shown in **Figure 2c** (see B) are the result of a processing or instrument error in the C-band HV channel.

Surface scattering is shown in blue and dominates a large portion of both scenes. Although there is some clear correlation between ice types and dominant scattering mechanism, volume scattering (shown in green) does not dominate an entire ice type in either frequency. For C-band data, volume scattering (green) is strongest in portions of MYI areas and in some areas of compressed ice (C) and leads (D). The latter could be an effect of the HV signal being masked in noise, although a volume component can be expected in thin ice (Nghiem et al., 1995). MYI regions show predominantly surface scattering for L-band (see E in **Figure 2d**). CFYI shows dominant volume scattering in L-band (see F in **Figure 2d**).

The application of a polarimetric filter (Lee et al., 1999a) is recommended for the subsequent classification. The averaging window results in spatial averaging, and the backscatter of a larger area compared with a single pixel is estimated. Pixels with dominating volume or dihedral scattering are averaged with neighbouring pixels where surface scattering is dominant. This results in an increase of the area with predominantly surface scattering (see **Figures 2e**, **2f**) for the filtered image. The application of a stronger filter (i.e., a larger filter window or additional multilooking) further increases this effect, so the filter strength needs to be carefully selected.

Wishart statistics based segmentation

Knowledge of the expected statistical distribution of a dataset allows the derivation of a classification approach that is optimal in the sense that, on average, its use yields the lowest probability for misclassification.

For multilook data, a maximum likelihood classification has been developed based on the Wishart distribution. Initial classes are derived using a training dataset in known terrain. The image is then classified according to the distance to the class means. Each pixel is assigned to the class to which it has the minimum distance. The distance itself is calculated to ensure that the Bayes maximum likelihood classification condition is satisfied (Lee et al., 1994). Details on the method are given in Appendix A.

The method is originally a supervised classifier, as training data are required. Lee et al. (1999b) show that the use of an unsupervised classifier to calculate initial class means to seed the Wishart statistics based segmentation provides an opportunity to reduce the level of interaction required.

The concept of classification using the Wishart statistics is illustrated in **Figure 3**. First, a polarimetric filter is used to reduce the effect of speckle for the pixel-based method. The edge-preserving filter developed by Lee et al. (1999a) was used on the data with a filter window size of five. The unsupervised classifier is used to provide the Wishart-based method with a seed classification, which is used to derive the initial class means. Using the Wishart-based method in iterations, these class means are updated after each iteration based on the resulting classification. The result is final after a preset number of iterations. Alternatively, the iterations could be terminated when the number of pixels changing class in an iteration is below a threshold. In this paper, three iterations are used ($n = 3$;

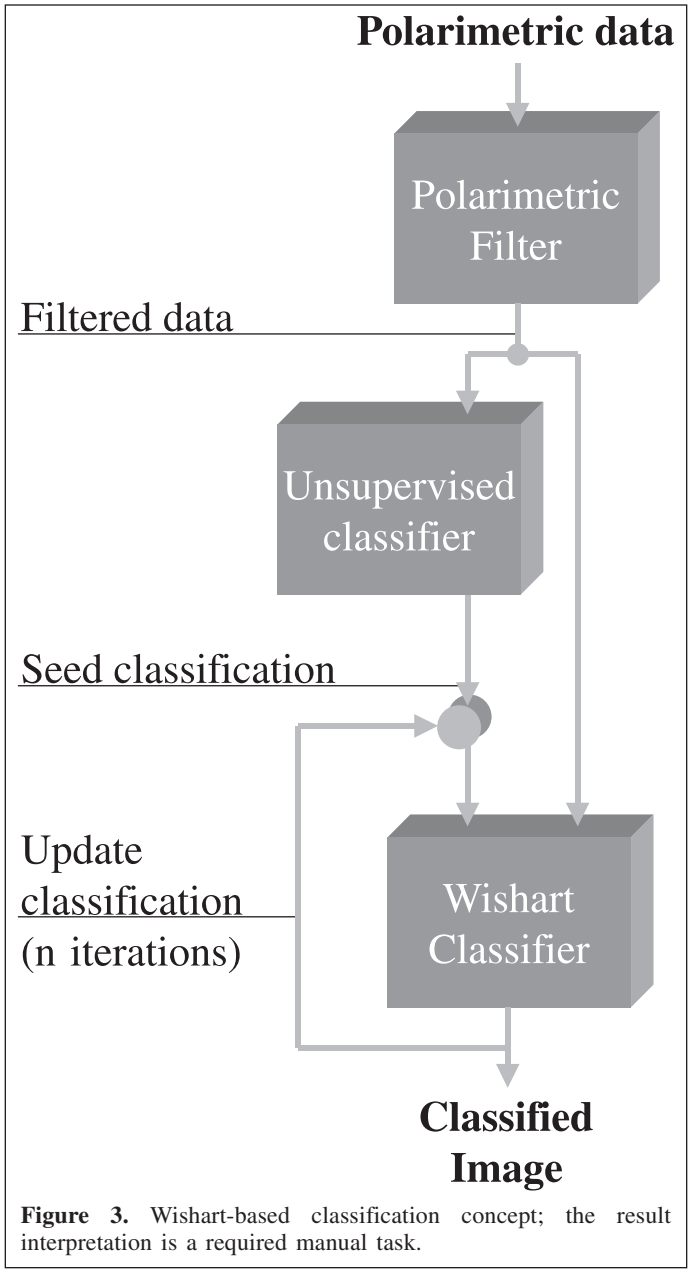

Figure 3. Wishart-based classification concept; the result interpretation is a required manual task.

see **Figure 3**). Often the sequential use of two different methods results in the requirement for manual class interpretation. Human interaction is then shifted from training data selection to result interpretation.

One unsupervised method often used is the entropy – anisotropy – alpha angle classifier (Cloude and Pottier, 1997). The method was extensively tested for sea ice by Scheuchl et al. (2001) and Scheuchl et al. (2002; 2003) using SIR-C, CV-580, and AirSAR data.

Scheuchl et al. (2003) suggest a slight modification of the entropy – alpha angle algorithm in the case of sea ice classification to accommodate particular numbers of classes rather than using the standard set of thresholds. This approach is appropriate, particularly as the class means change with iterations, and the final result is not related to the seed. The benefit of automated physical interpretation based on the entropy – alpha angle result is then no longer given, and manual result interpretation is required. The new approach leads to good results for a CV-580 dataset of sea ice when significant spatial averaging is applied.

For the AirSAR data used in this paper, the leads are not separated from smooth FYI when using the entropy – anisotropy – alpha angle seed method. Rodrigues et al. (2003) independently analyzed the dataset and showed similar results. The use of this method was therefore not considered in this paper.

Scheuchl et al. (2002) conclude that an image with *n* classes randomly distributed over the image can be used to seed the iterative Wishart-based method, resulting in a final result similar to that using entropy – anisotropy – alpha angle seed.

Lee et al. (2004) use the Freeman–Durden target decomposition (Freeman and Durden, 1998) to separate the dominant scattering mechanisms. The Wishart-based classifier is then applied separately for the three classes. Each class (or scattering mechanism) is divided into several subclasses based on signal strength. The subclasses are iterated using the Wishart-based classifier and can only change within one of the three scattering classes. The method was developed for land applications and shows promising results. The classification converges faster, causing fewer pixels to change class during an iteration. In addition, the interpretation of the main classes is given by the dominant scattering mechanism.

As discussed in the preceding section, the mix of scattering mechanisms is not very pronounced for sea ice. Surface scattering is strongest for most areas, and volume scattering is strongest for some areas of selected ice types depending on the radar frequency. Double bounce rarely dominates; filtering the data reduces the number of pixels with predominantly dihedral scattering even further. This domination of surface scattering reduces the information content of the approach compared to that of a land application.

Dual-frequency classification result (reference)

With dual-frequency data available, the combination of both frequencies is used to generate a reference result. Both frequencies show different signatures for sea ice, and the combined use leads to a better result compared with a single-frequency result. All single-frequency results are subsequently compared to this reference.

Figure 4 shows two dual-frequency classification results. A result from a previous study using a maximum a posteriori (MAP) classifier is shown in **Figure 4a** (Rignot and Drinkwater, 1994). **Figure 4b** shows the classification based on the Wishart distribution of the dual-frequency data. The classifier was seeded by using simple thresholds for the C-band total power image. C-band was selected because MYI is better identified in this dataset compared with L-band. A more detailed description of the seed option used is provided in the single-frequency result section. The two results shown in **Figure 4** correspond very well. The following discussion refers to the dual-frequency result based on the Wishart distribution.

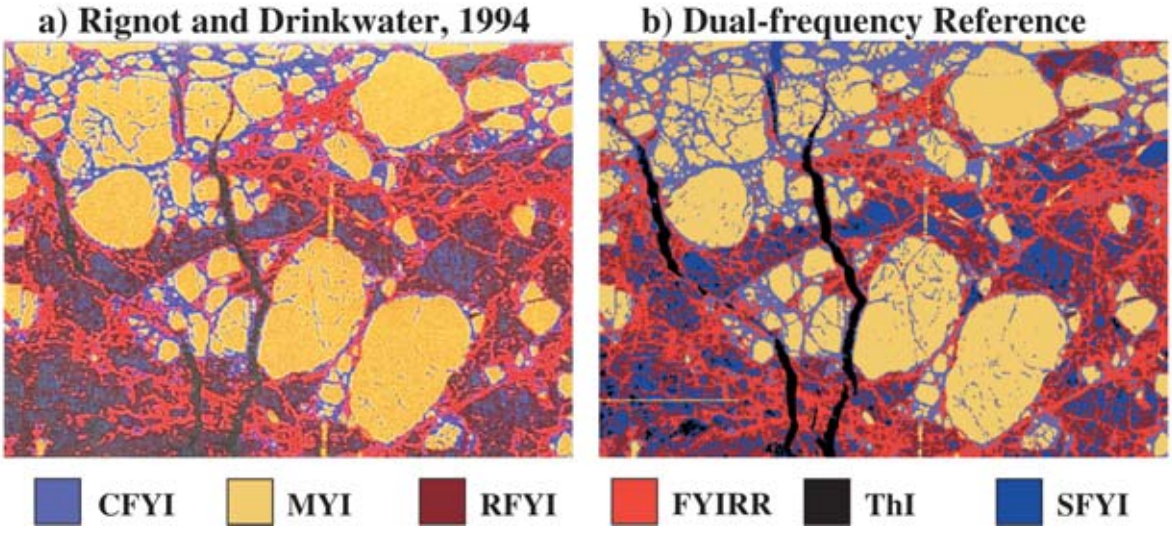

Figure 4. Dual-frequency (C- and L-band) fully polarimetric classification results. The comparison result taken from Rignot and Drinkwater (1994).

In this paper the number of classes was set to six based on a previous result. Another reason for this approach is that the number of ice types used in sea ice monitoring is limited. Open water, thin ice, FYI in various stages, and MYI are ice classes that can be identified in freezing conditions. A segmentation of six classes appears to be a reasonable tradeoff between number of classes and class interpretation effort. A more general approach would need to be evaluated using a much larger dataset and is outside the scope of this study.

Tables 1 and **2** show selected polarimetric parameters for each class of the reference result for C- and L-band, respectively. All parameters are estimated from the class mean (i.e., the averaged coherency matrix; see Appendix A). The classes are generally well separated by their backscatter strength (TP, HH, HV, and VV) but not necessarily by entropy, anisotropy, alpha angle, or copolarization-channel correlation magnitude. This leads to the conclusion that entropy, anisotropy, and alpha angle do not contain very much discrimination information for the investigated data.

All class means show dominant surface scattering. They represent the average of all pixels of one class. Spatial averaging (filtering) of the data shows a significant reduction in the proportion of volume scattering dominated pixels; calculating the class means leads to the same effect.

For C-band there is only a 0.5 dB difference between surface scattering (Ps) and volume scattering (Pv) for leads and 0.8 dB for CFYI, indicating a strong volume scattering component. MYI shows a 3 dB difference between Ps and Pv, and the other three classes differ by about 6 dB. Volume scattering dominating in large portions of the leads is an indication that the leads are in fact covered with thin ice. This result is in agreement with previously published analysis results for this dataset. Based on the Freeman–Durden model, there is some potential for error, since the system noise level is in the order of the backscatter signal for the cross-polarized channel. The Freeman–Durden model uses the cross-polarized signal to estimate the volume scattering component, and a noise level in the order of the cross-polarized signal backscatter is expected to falsify this estimation.

The L-band parameters show a more significant dominance of surface scattering. Here, the MYI floes have the weakest relative backscatter contribution (11.2 dB difference to Ps). Pv is relatively strong for CFYI (3.7 dB difference to Ps).

Entropy, anisotropy, alpha angle, and correlation magnitude are helpful in class interpretation; they support the information obtained from the Freeman–Durden model. Classes with a Ps to Pv ratio close to zero also show the highest entropy values, thus indicating the presence of several backscatter mechanisms of similar strength. The generally low alpha angle (<35°) shows the dominance of surface scattering.

Single-frequency classification results

With few dual-frequency sensors available to date, much interest lies in the capability of single-frequency data classification.

A simple classification based on signal strength was investigated and compared with the dual-frequency reference result (**Figure 5a**). The image was divided into initial classes based on total power (TP) to seed the Wishart-based segmentation. This approach was chosen because the data show predominantly surface scattering; the volume and dihedral part are simply not separated. **Figures 5b** and **5c** show the

Table 1. Dual-frequency result for C-band parameters estimated from the class mean.

Ice type	TP (dB)	Ps/Pv (dB)	Ps/Pd (dB)	HH (dB)	HV (dB)	VV (dB)	*H*	*A*	α (°)	|ρ|
CFYI	–6.5	0.8	9.2	–10.2	–19.2	–9.9	0.69	0.19	28.3	0.65
MYI	–7.7	3.1	10.7	–11.3	–21.8	–10.8	0.58	0.23	22.5	0.73
FYIRR	–13.3	5.2	9.6	–16.6	–29.1	–16.5	0.52	0.39	20.7	0.74
RFYI	–16.3	6.1	9.4	–19.4	–32.7	–19.5	0.50	0.47	19.1	0.74
SFYI	–18.6	6.1	8.8	–21.6	–35.1	–22.0	0.52	0.51	19.6	0.72
ThI	–23.5	0.5	5.4	–27.8	–36.4	–26.3	0.76	0.39	34.8	0.46

Note: *A*, anisotropy; *H*, entropy; HH and VV, copolarized channel intensity; HV, cross-polarized channel intensity; Pd, double bounce; Ps, surface scattering; PV, volume scattering; TP, total power; α, alpha angle; |ρ|, copolarized channel correlation magnitude.

Table 2. Dual-frequency result for L-band parameters estimated from the class mean.

Ice type	TP (dB)	Ps/Pv (dB)	Ps/Pd (dB)	HH (dB)	HV (dB)	VV (dB)	*H*	*A*	α (°)	|ρ|
CFYI	–8.9	3.7	22.2	–14.4	–23.2	–10.8	0.49	0.06	24.8	0.79
MYI	–15.1	11.2	20.1	–20.6	–35.6	–16.6	0.19	0.21	16.6	0.93
FYIRR	–13.6	5.6	13.4	–19.0	–29.4	–15.4	0.45	0.25	23.5	0.78
RFYI	–19.5	6.9	12.1	–25.0	–36.4	–21.1	0.42	0.37	23.8	0.77
SFYI	–25.1	7.5	11.4	–30.9	–42.6	–26.7	0.41	0.44	24.7	0.76
ThI	–30.4	5.0	11.9	–37.4	–45.8	–31.7	0.50	0.30	32.2	0.63

Note: Parameters defined as in **Table 1**.

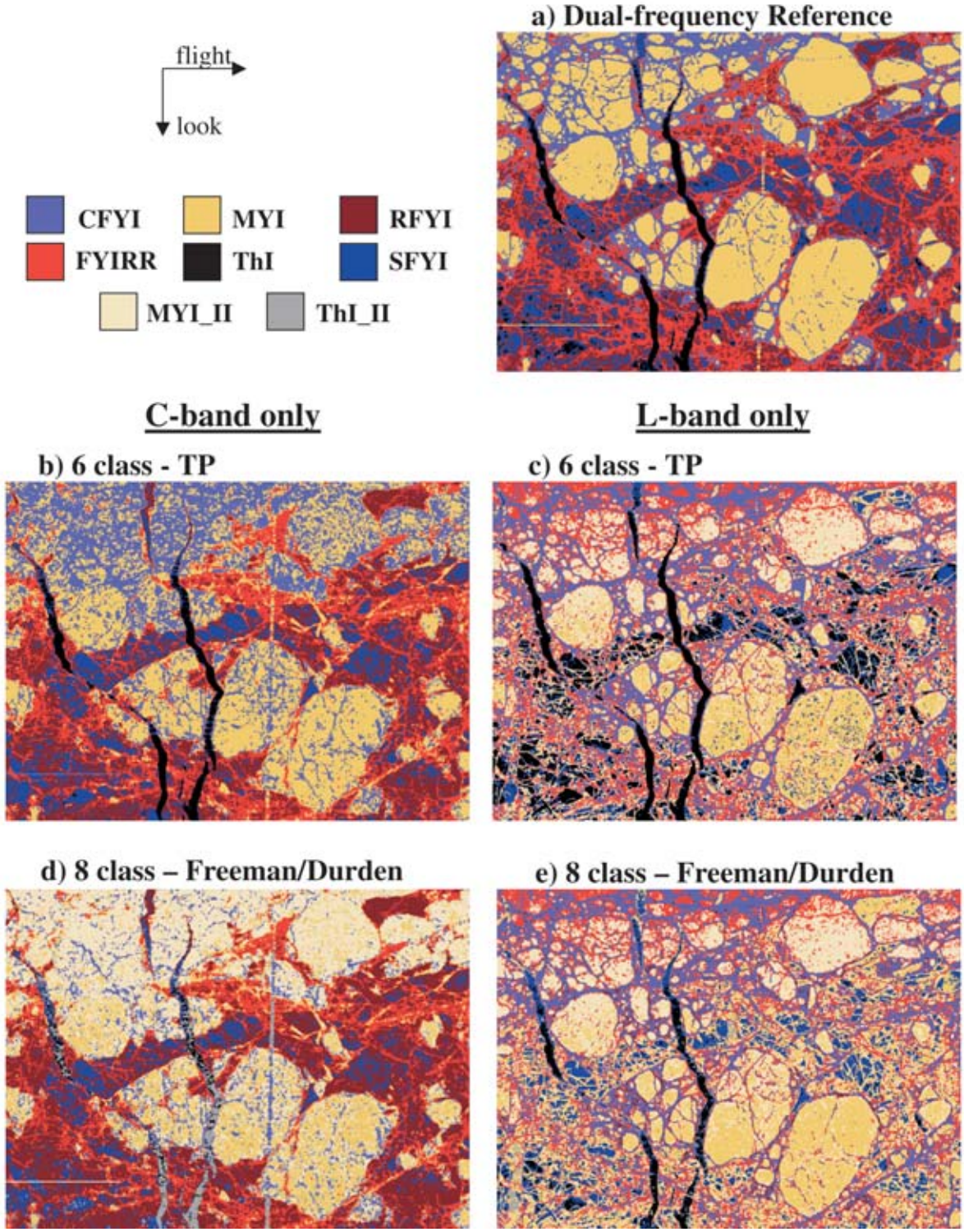

Figure 5. Single-frequency classification results using different seed options. Quantitative comparisons with the dual-frequency reference result are presented in **Tables 3–6**.

classification result based on the total power seed. Six classes were chosen in accordance with the reference result.

Figures 5d and **5e** show the classification result using the Freeman–Durden seed. With little dominant dihedral scattering available, only two scattering mechanisms, surface and volume scattering, were used to separate the data. Six surface scattering classes were used, as all classes of the reference result show surface scattering. Two volume scattering classes only were used, as dominant volume scattering was found for only a few ice types.

For both approaches, the initial class separation is based on nonuniformly separated signal strength levels. First, the data were divided in half using the median values for TP, Ps, and Pv. For TP and Ps, six classes were needed, which were implemented by dividing each of the two classes again using the median value for the class. The four resulting classes approximately cover the same number of pixels. Lastly, two more classes were created containing all pixels with the lowest 1% and 5% backscatter strength, respectively.

The low backscatter class approach is necessary to ensure that leads are identified. During the iterations, classes with low backscatter show a trend to grow with each iteration. Leads were not correctly identified using C-band data if the seed did not contain low backscatter classes.

Tables 3–6 show confusion matrices for the single-frequency results compared with the dual-frequency reference results.

Both C-band data results (**Figures 5b**, **5d**) show significant confusion between MYI and CFYI. There is clear indication that these two ice types cannot easily be separated using C-band data, which is also apparent from visual inspection of the RGB image (**Figure 1a**). The ridged and rough FYI classes (FYIRR and RFYI) also show confusion. If the two are combined into one class, which appears reasonable given the similarities (**Figure 1**), the classification accuracy would reach about 90%. Leads are underestimated, and a portion of the leads is classified as SFYI.

Applying the Freeman–Durden seed results in two additional segments, which carry some information. These segments do not represent separate ice types and need to be merged with other segments during interpretation. The additional effort required does not lead to a better classification result.

The L-band results (**Figures 5c**, **5e**) provide good information on the CFYI, which is also apparent from visual inspection of the RGB image (**Figure 1b**). Leads are overestimated in the total power seed approach; the Freeman–Durden seed result shows lead underestimation similar to that of the C-band results. An overestimation of MYI can be reported for both results. Multiple segments had to be merged to an MYI class (see **Tables 5** and **6**). The estimation of ridged and rough FYI is generally low (no RFYI was assigned).

In general, the use of Freeman–Durden as seed for the single-frequency Wishart-based segmentation requires the use of more classes. This results in an increased effort for data interpretation compared with the seed based on the total power. If the primary objective is the separation of the main ice types present in the scene, the use of the Freeman–Durden seed is not required. For the dataset at hand, there is very little benefit in a scattering mechanism separation for L-band. The C-band result based on the TP seed corresponds well to the RGB image (**Figure 1a**).

Both frequencies show limitations in their potential for ice-type separation, and the use of dual-frequency data leads to a better result. All single-frequency results show the influence of the incidence angle on the classification, which is not the case for the dual-frequency result.

Table 3. Confusion matrix of C-band TP seed compared with dual-frequency reference (given in % of the reference class).

Ice type	CFYI	MYI	FYIRR	RFYI	SFYI	ThI
CFYI	**60**	33	0	0	0	0
MYI	38	**66**	11	0	0	0
FYIRR	2	1	**75**	23	1	0
RFYI	0	0	14	**68**	43	0
SFYI	0	0	0	9	**55**	33
ThI	0	0	0	0	1	**67**

Note: The values in the diagonal shown in bold indicate the percentage of an ice type that is correctly classified.

Table 4. Confusion matrix of C-band Freeman–Durden seed compared with dual-frequency reference (given in % of the reference class).

Ice type	CFYI	MYI	FYIRR	RFYI	SFYI	ThI
CFYI	**25**	6	0	0	0	0
MYI[a]	69	**90**	9	0	0	0
FYIRR	2	1	**67**	15	1	0
RFYI	0	0	22	**80**	58	0
SFYI	0	0	0	4	**40**	35
ThI[a]	4	3	2	1	1	**65**

[a]Formed from two different segments.

Table 5. Confusion matrix of L-band TP seed compared with dual-frequency reference (given in % of the reference class).

Ice type	CFYI	MYI	FYIRR	RFYI	SFYI	ThI
CFYI	**83**	0	23	0	0	0
MYI[a]	17	**54**	72	43	0	0
FYIRR	0	44	**5**	41	0	0
RFYI[b]	—	—	—	—	—	—
SFYI	0	2	0	16	**59**	0
ThI	0	0	0	0	41	**100**

[a]Formed from two different segments.
[b]Not classified.

Table 6. Confusion matrix of L-band Freeman–Durden seed compared with dual-frequency reference (given in % of the reference class).

Ice type	CFYI	MYI	FYIRR	RFYI	SFYI	ThI
CFYI	**76**	0	31	0	0	0
MYI[a]	11	**77**	6	90	36	0
FYIRR	12	23	**61**	4	0	0
RFYI[b]	—	—	—	—	—	—
SFYI	0	0	0	0	**60**	38
ThI[c]	1	0	2	2	3	**62**

[a]Formed from three different segments.
[b]Not classified.
[c]Formed from two different segments.

The application of iterations for the Wishart-based segmentation is recommended because this improves the seed result significantly. For C-band data, both Freeman–Durden and total power seed show better results than the entropy – anisotropy – alpha angle seeded result (not shown here). In addition to leads being identified, the iterative Wishart-based

approach converges much faster, thus requiring fewer iterations (n = 3 used here) and less processing time.

The results shown are based on a single scene and cannot easily be generalized. The data were acquired in freezing conditions. Surface melt or a wet snow layer on the ice are much more challenging environmental conditions. In such a case, the signatures of the sea ice types would largely be masked by the surface conditions, making classification extremely difficult. No such dataset was available for analysis, and the issue needs to be addressed in the future when data can be acquired over an entire ice season.

Data calibration issues

Data calibration is not a critical issue for the Wishart-based method discussed because it relies on relative comparison only. The method compares each pixel to a set of classes derived from the dataset itself. The initial classification may change based on calibration quality, in particular if scattering mechanism based approaches like the Freeman–Durden or entropy – anisotropy – alpha angle approaches are used. These parameters are expected to be more sensitive to data calibration than the segmentation process. Calibration requirements posted for other applications (Freeman, 1992) meet or exceed the requirements for the application of the Wishart-based method.

One issue that is of interest for spaceborne systems is the system noise level (noise equivalent sigma nought or NESZ) and more importantly any variation of the NESZ over the image swath. There is usually more system noise present in a spaceborne system than in an airborne system. Backscatter from sea ice is generally lower than that from land areas, and cross-polarized backscatter is about 10 dB lower than copolarization backscatter. Cross-polarized ice signatures can be below –25 dB (see **Tables 1** and **2**), which is close to or below proposed system noise levels for current and upcoming spaceborne missions. If the noise level varies significantly over the swath, the classifier will be affected. The availability of accurate information on the NESZ variation and the development of a classification concept considering this information are recommended.

Conclusions

Synthetic aperture radar (SAR) instruments are an important information source for high-resolution sea ice monitoring. Sea ice represents a challenging target because it undergoes a seasonal cycle, with the melt season presenting the most challenging conditions for classification.

A classification scheme based on the Wishart distribution of polarimetric data is a versatile tool applicable to fully polarimetric single-frequency and multifrequency SAR data. A semisupervised approach was investigated here for polarimetric SAR data of sea ice (class assignment to ice types is a required manual task).

Sea ice has less variation in its composition of backscatter than land. Surface scattering is dominant for most of the test data. Volume scattering only dominates parts of selected ice types like thin ice and compressed first-year ice (in the case of C-band, also MYI). Dihedral scattering is dominant only for a few pixels, and speckle filtering further reduces this number.

The use of a Freemen–Durden seed for the Wishart-based segmentation, developed and successfully applied for land applications, does not necessarily improve the classification result. Although some additional information is available for image interpretation, a very simple backscatter strength based seed provides satisfactory results with fewer classes, thus requiring less interpretation.

Generally, a backscatter strength based seed requires fewer iterations of the Wishart classifier compared with the entropy – alpha angle seed. Each single-frequency result shows some class confusion compared with the reference result, indicating radar wavelength dependent limitations for ice type separation. Applied to dual-frequency data, the method can utilize the different information content of both frequencies. The result clearly outperforms single-frequency classification.

Acknowledgements

The AirSAR data were provided by the NASA JPL, and the authors are grateful to Ben Holt (JPL) and Eric Rignot for their help in retrieving the data. Ron Caves (MacDonald Dettwiler and Associates Ltd.) and Dean Flett (CIS) provided valuable information on data analysis and ice interpretation, respectively. The authors thank the anonymous reviewers for their constructive feedback.

References

Cloude, S.R., and Pottier, E. 1997. An entropy based classification scheme for land applications of polarimetric SAR. *IEEE Transactions on Geoscience and Remote Sensing*, Vol. 35, No. 1, pp. 68–78.

Drinkwater, M.R., Kwok, R., Winebrenner, D.P., and Rignot, E. 1991. Multifrequency polarimetric synthetic aperture radar observations of sea ice. *Journal of Geophysical Research*, Vol. 96, No. C11, pp. 20 679 – 20 698.

Drinkwater, M.R., Kwok, R., Rignot, E., Israelsson, H., Onstott, R.G., and Winebrenner, D.P. 1992. Potential applications of polarimetry to the classification of sea ice. In *Microwave remote sensing of sea ice*. Edited by F. Carsey. American Geophysical Union, Geophysical Monograph 68, pp. 419–430.

Eriksson, L., Drinkwater, M., Holt, B., Valjavek, E., and Nortier, O. 1998. SIR-C polarimetric radar results from the Weddell Sea, Antarctica. In *IGARSS'98, Proceedings of the International Geoscience and Remote Sensing Symposium*, 6–10 July 1998, Seattle, Wash. IEEE, New York. pp. 2222–2224.

Ferro-Famil, L., Pottier, E., and Lee, J.S. 2001. Unsupervised classification of multifrequency and fully polarimetric SAR images based on the H/A/Alpha–Wishart classifier. *IEEE Transactions on Geoscience and Remote Sensing*, Vol. 39, No. 11, pp. 2332–2342.

Freeman, A. 1992. SAR calibration: an overview. *IEEE Transactions on Geoscience and Remote Sensing*, Vol. 30, No. 6, pp. 1145–1149.

Freeman, T., and Durden, S.L. 1998. A three-component scattering model for polarimetric SAR data. *IEEE Transactions on Geoscience and Remote Sensing*, Vol. 36, No. 3, pp. 963–973.

Hallikainen, M., and Winebrenner, D.P. 1992. The physical basis for sea ice remote sensing. In *Microwave remote sensing of sea ice*. Edited by F. Carsey. American Geophysical Union, Geophysical Monograph 68. pp. 29–46.

Kong, J.A., Swartz, A.A., Yueh, H.A., Novak, L.M., and Shin, R.T. 1988. Identification of terrain cover using the optimal polarimetric classifier. *Journal of Electromagnetic Waves and Applications*, Vol. 2, pp. 171–194.

Kwok, R., Nghiem, S.V., Yueh, S.H., and Huynh, D.D. 1995. Retrieval of thin ice thickness from multifrequency polarimetric SAR data. *Remote Sensing of Environment*, Vol. 51, pp. 361–374.

Lee, J.-S., Grunes, M., and Kwok, R. 1994. Classification of multi-look polarimetric SAR imagery based on complex Wishart distribution. *International Journal of Remote Sensing*, Vol. 15, No. 11, pp. 2299–2311.

Lee, J.-S., Grunes, R., and de Grandi, G. 1999a. Polarimetric SAR speckle filtering and its implication for classification. *IEEE Transactions on Geoscience and Remote Sensing*, Vol. 37, No. 5, pp. 2363–2373.

Lee, J.-S., Grunes, M.R., Ainsworth, T.L., Du, L.-J., Schuler, D.L., and Cloude, S.R. 1999b. Unsupervised classification using polarimetric decomposition and the complex Wishart classifier. *IEEE Transactions on Geoscience and Remote Sensing*, Vol. 37, No. 5, pp. 2249–2258.

Lee, J.-S., Grunes, M.R., Pottier, E., and Ferro-Famil, L. 2004. Unsupervised terrain classification preserving polarimetric scattering characteristics. *IEEE Transactions on Geoscience and Remote Sensing*, Vol. 42, No. 4, pp. 722–731.

Nghiem, S.V., and Bertoia, C. 2001. Study of multi-polarization C-band backscatter signatures for arctic sea ice mapping with future satellite SAR. *Canadian Journal of Remote Sensing*, Vol. 27, No. 5, pp. 387–402.

Nghiem, S.V., Kwok, R., Yueh, S.H., and Drinkwater, M.R. 1995. Polarimetric signatures of sea ice 2. Experimental observations. *Journal of Geophysical Research*, Vol. 100, No. C7, pp. 13 681 – 13 698.

Rignot, E., and Drinkwater, M.R. 1994. Winter sea-ice mapping from multiparameter synthetic aperture radar. *Journal of Glaciology*, Vol. 40, No. 134, pp. 31–45.

Rignot, E., Chellappa, R., and Dubois, P. 1992. Unsupervised segmentation of polarimetric SAR data using the covariance matrix. *IEEE Transactions on Geoscience and Remote Sensing*, Vol. 30, No. 4, pp. 697–705.

Rodrigues, A., Corr, D., Partington, K., Pottier, E., and Ferro-Famil, L. 2003. Unsupervised Wishart classifications of sea-ice using entropy, alpha and anisotropy decompositions. In *POLinSAR 2003, Proceedings of the Workshop on Application of SAR Polarimetry and Polarimetric Interferometry*, 14–16 January 2003, Frascati, Italy. POLINSAR Proceedings SP-529, ESA Publications Division, Noordwijk, The Netherlands.

Scheuchl, B., Caves, R., Cumming, I., and Staples, G. 2001. H/A/α-based classification of sea ice using SAR polarimetry. In *Proceedings of the 23rd Canadian Symposium on Remote Sensing*, 21–24 August 2001, Québec City, Que. Canadian Aeronautics and Space Institute, Ottawa, Ont.

Scheuchl, B., Hajnsek, I., and Cumming, I. 2002. Sea ice classification using multi-frequency polarimetric SAR data. In *IGARSS'02*, *Proceedings of the International Geoscience and Remote Sensing Symposium*, 24–28 June 2002, Toronto, Ont. IEEE, New York.

Scheuchl, B., Hajnsek, I., and Cumming, I. 2003. Classification strategies for polarimetric SAR sea ice data. In *POLinSAR 2003, Proceedings of the Workshop on Application of SAR Polarimetry and Polarimetric Interferometry*, 14–16 January 2003, Frascati, Italy. POLINSAR Proceedings SP-529, ESA Publications Division, Noordwijk, The Netherlands.

Scheuchl, B., Flett, D., Caves, R., and Cumming, I. 2004. Potential of RADARSAT-2 data for operational sea ice monitoring. *Canadian Journal of Remote Sensing*, Vol. 30, No. 3, pp. 448–461.

Winebrenner, D.P., Farmer, L.D., and Joughin, I.R. 1995 On the response of polarimetric SAR signatures at 24 cm wavelength to sea ice thickness in Arctic leads. *Radio Science*, Vol. 30, No. 2, pp. 373–402.

Appendix A. Wishart-based segmentation

Multilook polarimetric data can be described using the coherency matrix **T**. **T** has a complex Wishart distribution and is formed from a vectorization, $\boldsymbol{k}_{\mathbf{T}}$, of the scattering matrix **S**:

$$\mathbf{T} = \boldsymbol{k}_{\mathbf{T}} \cdot \boldsymbol{k}_{\mathbf{T}}^{+} \qquad \text{where } \boldsymbol{k}_{\mathbf{T}} = \frac{1}{\sqrt{2}} \begin{pmatrix} S_{\mathrm{HH}} + S_{\mathrm{VV}} \\ S_{\mathrm{HH}} - S_{\mathrm{VV}} \\ 2S_{\mathrm{HV}} \end{pmatrix} \tag{A1}$$

where S_{HH}, S_{HV}, and S_{VV} are elements of **S**. The superscript + indicates conjugate complex. **T** is closely related to the covariance matrix **C**, and the matrices can be interchanged in the equations to follow.

For multilook data, a maximum likelihood supervised classification has been developed based on the Wishart distribution. Initial classes are derived using a training dataset in known terrain. The image is then classified according to the distance to the class means. Each pixel is assigned to the class to which it has the minimum distance. The distance itself is calculated to ensure that the Bayes maximum likelihood classification condition is satisfied (Lee et al., 1994). A look-independent distance measure, d, can then be written as

$$d(\langle \mathbf{T} \rangle, \mathbf{V}_{\mathrm{m}}) = \ln|\mathbf{V}_{\mathrm{m}}| + \mathrm{Trace}(\mathbf{V}_{\mathrm{m}}^{-1} \langle \mathbf{T} \rangle) \tag{A2}$$

where $\langle \mathbf{T} \rangle$ is the n-look coherency matrix, and Trace is the sum of the elements in the main diagonal of a matrix. The class mean $\boldsymbol{V}_{\mathrm{m}}$ is defined as follows:

$$\mathbf{V}_{\mathrm{m}} = E\{\langle \mathbf{T} \rangle | \langle \mathbf{T} \rangle \in \omega_m\} \tag{A3}$$

where ω_m is the set of pixels belonging to class m, and $E\{.\}$ is the expected value and can be estimated as the class average.

A pixel is assigned to a certain class if the distance between the pixel and the class mean is minimum:

$$d(\langle \mathbf{T} \rangle, \mathbf{V}_{\mathrm{m}}) \leq d(\langle \mathbf{T} \rangle, \mathbf{V}_j) \quad \text{for all} \quad \omega_j \neq \omega_m \tag{A4}$$

The look independence of this scheme allows its application to multilooked and speckle-filtered data.

This classification scheme can be generalized for multifrequency, fully polarimetric data (Lee et al., 1994; Ferro-Famil et al., 2001), provided that the frequencies are sufficiently separated to ensure statistical independence

between frequency bands. Also, the data from different bands need to be properly coregistered in this case. The multifrequency distance measure can be defined as the sum

$$d(\langle \mathbf{T}_1 \rangle \ldots \langle \mathbf{T}_n \rangle, \mathbf{V}_m) = \sum_k d(\langle \mathbf{T}_k \rangle, \mathbf{V}_m) \quad \text{(A5)}$$

where $k = [1, n]$ denotes the frequency bands used.